Material and Morphology Parameter Sensitivity Analysis in Particulate Composite Materials

Xiaoyu Zhang* and Caglar Oskay†

Department of Civil and Environmental Engineering
Vanderbilt University
Nashville, TN 37212

05/25/2017

Abstract

This manuscript presents a novel parameter sensitivity analysis framework for damage and failure modeling of particulate composite materials subjected to dynamic loading. The proposed framework employs global sensitivity analysis (GSA) to study the variance in the failure response as a function of model parameters. In view of the computational complexity of performing thousands of detailed microstructural simulations to characterize sensitivities, Gaussian Process (GP) surrogate modeling is incorporated into the framework. In order to capture the discontinuity in response surfaces, the GP models are integrated with a support vector machine (SVM) classification algorithm that identifies the discontinuities within response surfaces. The proposed framework is employed to quantify variability and sensitivities in the failure response of polymer bonded particulate energetic materials under dynamic loads to material properties and morphological parameters that define the material microstructure. Particular emphasis is placed on the identification of sensitivity to interfaces between the polymer binder and the energetic particles. The proposed framework has been demonstrated to identify the most consequential material and morphological parameters under vibrational and impact loads.

Keywords: Energetic materials interfaces, Surrogate model, Global Sensitivity Analysis

*Author address: 1102 17th Avenue South, Nashville, TN 37212. Email: xiaoyu.zhang@vanderbilt.edu
†Corresponding author address: 1102 17th Avenue South, Nashville, TN 37212. Email: caglar.oskay@vanderbilt.edu

1 Introduction

Dynamic behavior of particulate composites such as energetic materials subjected to high amplitude, transient (e.g., harmonic or shock) loads is often complicated due to interacting chemo-thermo-mechanical processes acting at multiple time and length scales. A significant body of work exists on understanding and characterization of the roles of various mechanisms (e.g., pore collapse, intergranular friction, particle fracture, interface debonding, dislocation pile-ups [3, 13, 59]) to the overall composite performance. The corresponding mechanistic models that describe the constituent (e.g., binder, particle, interfaces, particle-particle interactions) behavior reflect the degree of complexity of these mechanisms [60]. In mesoscale simulations with tremendously complex morphologies and material behavior, characterization of the relative roles of the competing and interacting deformation and failure mechanisms is a significant challenge. This manuscript describes a computational sensitivity analysis framework to quantify the parametric and morphological sensitivity of particulate composites subjected to dynamic loading.

A number of sensitivity analysis techniques including One-At-a-Time (OAT) [43], screening methods [31], differential analysis/local methods [38], scatter plot [32], regression analysis [5], global sensitivity analysis [45], among others [6, 44] have been developed in the past several decades (see e.g., [44] for an overview). Among these methods, OAT, differential analysis, and regression analysis have been previously used to capture parameter sensitivity in particulate composites. In energetic materials, sensitivity analyses have been largely performed using the OAT method, which probes the vicinity of a calibrated parameter set by varying one parameter at a time while other parameters are kept constant. Czerski and Proud [9] applied the OAT method on cyclotrimethylene-trinitramine to investigate its shock sensitivity to particle size and particle morphologies. Barua et al. [2] investigated the ignition sensitivity of granular explosives (GXs) and polymer-bonded explosives (PBXs) to morphology (grain volume fraction, grain size distribution) and impact velocity. One main drawback of the OAT method is the inability of accounting for the interactions between parameters since only one parameter is probed each time [43].

Differential analysis relies on (typically numerical) differentiation of the response function with respect to each input parameter [22]. For instance, Rohan and Miara [40] derived analytical sensitivity formulae for the homogenized properties of particle reinforced piezoelectric composites with respect to parameters that control particle morphology. The resulting sensitivities obtained in differential analysis are local, and the overall sensitivity of a response function to an input variable is not readily available. Furthermore, this approach is typically applicable and feasible for simple and smooth response functions, in which differentiation is possible. Numerical approaches to differentiation are often computationally costly and limited

to obtaining local sensitivities [19]. Regression analysis has also been employed as a sensitivity analysis method [5, 55] including for particulate composites. For instance, Seuntjens et al. [48] calculated a Partial Rank Correlation Coefficient (PRCC), a rank regression parameter, to rank the sensitivities of physical and chemical properties that affect transport in porous particulate media. Regression analysis relies on an assumed relationship between inputs and outputs, which makes the obtained results dependent upon the assumed functional form [6].

Global sensitivity analysis (GSA) methods offer the capability to exploit the entire parameter space, and are able to probe beyond small local subspaces. For instance, Yu et al. [64] employed a GSA-based high dimensional model representation (HDMR) method to assess the sensitivity of mesoscale parameters on the elastic properties of a particulate composite. The capability of exploring the entire parameter space is one of the main reasons that GSA has a better chance to avoid misclassification of a highly sensitive parameter as non-influential (or vice-versa). GSA methods also account for the interaction terms between input parameters [45].

In this manuscript, a computational sensitivity analysis framework is developed to quantify the material and morphological sensitivities in the dynamic response of particulate composites. The proposed analysis framework is based on global sensitivity analysis (GSA) coupled with Gaussian Process (or Kriging) Surrogate Modeling for computational efficiency. The proposed framework is verified in the context of the dynamic response of Hydroxyl-terminated polybutadiene (HTPB) polymeric binder reinforced with ammonium perchlorate (AP) particles. Analyses were performed to quantify sensitivities of material (particularly interfacial) and morphological parameters on the AP-HTPB composites subjected to impact and harmonic loads.

The execution of GSA requires a substantial number of forward simulations, particularly for highly varying response functions. The nonlinear dynamic simulations of particulate composite mesostructures [66] are typically extremely costly from the computational perspective. In order to perform sensitivity analysis in a computationally efficient manner, the present manuscript relies on surrogate (i.e., Gaussian Process) modeling of the dynamic thermo-mechanical behavior of the material mesostructure. Gaussian Process (GP) models employing commonly used squared exponential kernel or rational quadratic kernels are well-known to exhibit significant errors when the response function has discontinuities [52]. A novel contribution of this manuscript is the development of a piece-wise continuous GP model to represent discontinuous response functions. The piece-wise continuous GP model is built by employing the support vector machine (SVM) - a classification algorithm [7]. Instead of using the representative response surface generated by global surrogate model trained over the entire input domain,

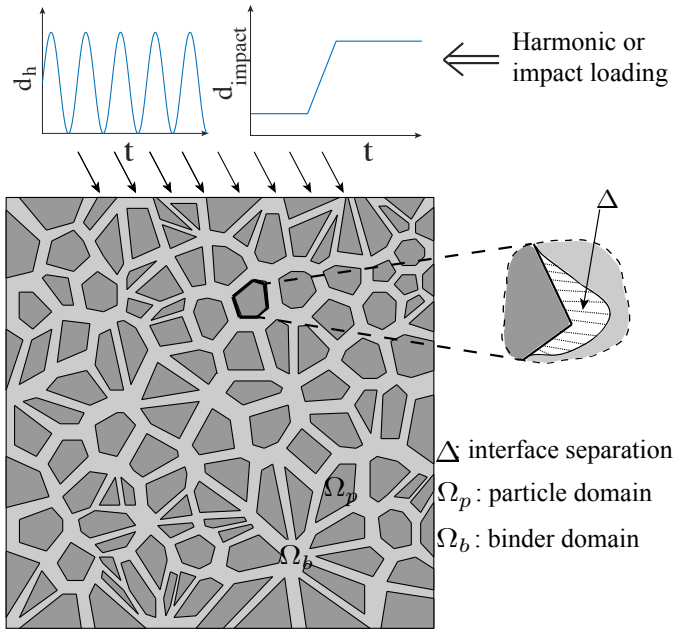

Figure 1: Problem setting: mesoscale geometry and loading.

several local surrogate models are generated for different parameter subdomains to capture the response surface, and SVM is utilized to identify the parameter subdomains.

The remainder of this manuscript is structured as follows: Section 2 provides the problem setting and the material models employed in the forward simulation of the dynamic response of particulate composites at the mesoscale. Section 3 describes of the proposed sensitivity analysis framework, including the piece-wise continuous GP surrogate model, the support vector machine classifier and the global sensitivity analysis method. Numerical examples that utilize the proposed framework to quantify the sensitivity of material properties and mesoscale geometry parameters are discussed in Section 4. Section 5 provides a summary and the conclusions.

2 Meso-scale Modeling of the AP-HTPB system

We are interested in computing the sensitivity of the dynamic response of a mesoscale representative volume to material parameters of the composite constituents as well as the mesoscale morphology. Consider a representative volume that consists of randomly positioned particles with varying particle sizes and shapes as illustrated in Fig. 1. Under the applied loading, the composite is taken to undergo dissipative, large thermo-mechanical deformations. In order to limit the complexity of the physics involved, the amplitude of the loads are taken small enough and possible chemical reactions are excluded. The interfaces between the particles and the binder are allowed to progressively degrade and debond. In view of the short loading

times, the thermal process within the representative volume is assumed to be adiabatic. The particles are taken to exhibit elastic behavior under the applied loading. The constitutive models of the binder and the interfaces are described below.

2.1 Binder Constitutive Model

The binder is taken to be significantly softer than the particles, and assumed to exhibit viscoelastic response [20, 62]. The Cauchy stress within the binder is expressed in terms of the hereditary integral as a function of the shear relaxation modulus as

$$\boldsymbol{\sigma} = \int_0^t 2G(t,\tau)\boldsymbol{D}'(\tau)d\tau + K\frac{\ln J}{J}\boldsymbol{\delta} \tag{1}$$

where, $\boldsymbol{D}'(\tau)$ is the deviatoric component of the deformation-rate tensor, $\boldsymbol{D} = (\boldsymbol{L}^T + \boldsymbol{L})/2$, with $\boldsymbol{L}$ the velocity gradient tensor ($\boldsymbol{L} = \dot{\boldsymbol{F}}\boldsymbol{F}^{-1}$ with $\boldsymbol{F}$ the deformation gradient tensor), and $G(t,\tau)$ the shear relaxation modulus. The volumetric part of the deformation is taken to behave elastically and K is the bulk modulus. J is the determinant of the deformation gradient, and $\boldsymbol{\delta}$ is the Kronecker delta.

The shear relaxation modulus, $G(t,\tau)$, is idealized using the Prony Series representation:

$$G(t,\tau) = \frac{T(\tau)}{T_{\text{ref}}}G_{h\infty}\left[1 + \sum_{i=1}^{n} p_i \exp\left(\frac{-(\xi(t) - \xi(\tau))}{q_i}\right)\right] \tag{2}$$

where, $G_{h\infty}$ is the steady-state shear modulus of the binder, T the temperature, T_{ref} the reference temperature, p_i and q_i are the fitting parameters of the n pairs of Prony Series prescribing the relative modulus, the relaxation time of the i_{th} Prony Series term, respectively, and:

$$\xi(t) = \int_0^t \frac{1}{a(T(\tau))}d\tau \tag{3}$$

where, $a(T)$ is the Williams-Landel-Ferry (WLF) empirical time-temperature shift function:

$$\log(a(T)) = \frac{A(T - T_{\text{ref}})}{B + T - T_{\text{ref}}} \tag{4}$$

A and B are material parameters. In view of the low conductivity and short loading time, the thermal process within the representative volume is assumed to be adiabatic. The viscoelastic dissipation induced heating under the adiabatic assumption is given by:

$$\dot{T} = \frac{1}{C_{V_b}\dot{W}_d} = \frac{2G_{h\infty}}{C_{V_b}}\frac{T(t)}{T_{\text{ref}}}\sum_{i=1}^{n}\frac{p_i}{q_i}\boldsymbol{\varepsilon}_d^i(t) : \boldsymbol{\varepsilon}_d^i(t) \tag{5}$$

where W_d is the dissipated work per unit reference volume, C_{V_b} the heat capacity per reference volume, and

$$\boldsymbol{\varepsilon}_d^i(t) = \int_0^t \exp\left(\frac{-(\xi(t) - \xi(\tau))}{q_i}\right) \boldsymbol{D}'(\tau) d\tau \tag{6}$$

2.2 Interface Constitutive Model

Prior experimental studies (e.g., [39, 65]) demonstrated that debonding at particle/binder interfaces is an important failure mechanism that may result in localized hot-spots in the context of energetic composites. Progressive damage accumulation and interface fracture is modeled by employing Cohesive Zone Modeling (CZM). CZM is well-known to accurately describe fracture processes particularly when the fracture path is pre-defined such as in the case of interface debonding problems [12].

In this manuscript, a bilinear traction-separation law is employed in the context of CZM following Ref. [20]. Let $\lambda(\mathbf{x})$ denote a normalized equivalent displacement jump measure at an interface point, $\mathbf{x} \in S$ defined as [57]:

$$\lambda = \begin{cases} \sqrt{(\frac{\Delta_n}{\Delta_{cn}})^2 + (\frac{\Delta_t}{\Delta_{ct}})^2}, & \Delta_n \geq 0 \\ \frac{|\Delta_t|}{\Delta_{ct}}, & \Delta_n < 0 \end{cases} \tag{7}$$

where Δ_n and Δ_t are the normal and tangential components of the separation vector; and Δ_{cn} and Δ_{ct} are the critical normal and critical tangential separations under pure mode I and mode II conditions, respectively that result in traction free surface. Let λ_{ul} denote a history variable describing the peak normalized separation measure throughout the loading history:

$$\lambda_{ul} = \max_{\tau \in [0,t]} \lambda(\tau) \tag{8}$$

The damage state, d_m, at a material point is then expressed as a function of the history variable:

$$d_m = \begin{cases} 0, & 0 \leq \lambda_{ul} \leq \eta_0 \\ \frac{\lambda_{ul} - \eta_0}{(1-\eta_0)\lambda_{ul}}, & \eta_0 < \lambda_{ul} \leq 1 \\ 1, & \lambda > 1 \end{cases} \tag{9}$$

in which, η_0 is the elastic separation limit. The traction-separation relationship is expressed as a function of damage, d_m, as:

$$t_{nc} = (1 - d_m) \frac{T_{\max}}{\eta_0} \frac{\Delta_n}{\Delta_{cn}} \tag{10}$$

$$t_{tc} = (1 - d_m) \frac{T_{\max}}{\eta_0} \frac{\Delta_t}{\Delta_{ct}} \tag{11}$$

where, t_{nc} and t_{tc} are normal and tangential traction components; $T_{\max}$ denotes the maximum interfacial traction.

The interpenetration between binder and particle is prevented by using the penalty contact algorithm. A linear relation between interpenetration ($|\Delta_n|$) and penalty traction p_n is:

$$p_n = \beta_p |\Delta_n| H(-\Delta_n) \tag{12}$$

where β_p is the penalty parameter; and H the Heaviside function. A regularized Coulomb law is employed to model the post-debonding frictional behavior along the particle-binder interface:

$$t_{tf} = \mu \frac{\dot{\Delta}_t}{\sqrt{\dot{\Delta}_t^2 + (\epsilon)^2}} |p_n| \tag{13}$$

where ϵ is a regularization parameter, and as it approaches zero, Eq. 13 recovers the classical Coulomb law.The superposed dot indicates material time derivative. μ is the friction coefficient that increases with accumulating damage:

$$\mu = d_m \, \mu_0 \tag{14}$$

The overall local normal and tangential tractions considering the cohesive and the contact behavior are expressed as:

$$\boldsymbol{t}_n = [H(\Delta_n) t_{nc} + (H(\Delta_n) - 1) p_n] \hat{\boldsymbol{n}} \tag{15}$$

$$\boldsymbol{t}_t = [t_{tc} + (1 - H(\Delta_n)) t_{tf}] \hat{\boldsymbol{t}} \tag{16}$$

where $\hat{\boldsymbol{n}}$ and $\hat{\boldsymbol{t}}$ are the normal and tangential unit vectors at the interface point. The decohesion process is assumed to generate negligible heat compared to the interface frictional heat. The total dissipated energy rate at the interface is assumed to be due to friction alone, which in turn leads to adiabatic temperature change as:

$$\dot{T}_{\text{int}} = \frac{t_{tf} \dot{\Delta}_t}{C_{V_{\text{int}}}} \tag{17}$$

where $C_{V_{\text{int}}}$ is the specific heat capacity at the interface.

2.3 Mesoscale Geometry

The morphology of the particulate composite mesostructure significantly affects the failure and initiation behavior in energetic materials [23, 24, 30, 58]. Despite the recognition of morphology as a key factor influencing material dynamic behaviors, the relative importance/sensitivities of

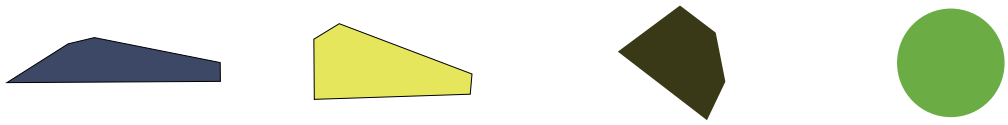

(a) $s = 0.62$ (b) $s = 0.75$ (c) $s = 0.85$ (d) $s = 1$

Figure 2: Shapes with different sphericity.

morphological parameters with respect to the behavior of interest remains to be systematically investigated and quantified. In the current study, the mesoscale morphology is probabilistically parameterized by the following: (1) particle size distribution, (2) particle area fraction distribution, and (3) particle sphericity (i.e., particle shape) distribution.

The particle area fraction and size distribution significantly affect the particle/binder interfacial behavior and the interaction between particles [1, 34]. For instance, the burning rate tailorability of propellants and explosive materials is partially controlled by particle size distributions [56]. In this study, the size of a particle is quantified directly as the area occupied by the particle.

Energetic particles vary significantly in shape and complexity which directly influence the particle-particle and particle-binder interactions. The impact of particle shape in localized increases in temperature has been reported in Refs. [11, 23, 30]. In the current manuscript, particle shapes are idealized as polygons, and the shape distribution is defined by the distribution of the parameter "sphericity". The sphericity is defined as the ratio of the perimeter of a sphere with equivalent particle size to perimeter of the polyhedron:

$$s = \frac{P_{eq}}{L_{edge}} \tag{18}$$

where $P_{eq} = 2\sqrt{\pi A}$, with A the particle size, L_{edge} the perimeter of the polyhedron. The sphericity value for each particle varies in the range $(0, 1)$. Sphericity near zero represents a thin and long shape, while near unit sphericity represents a shape that is very similar to a circle. Different shapes controlled by different sphericities are illustrated in Fig. 2. In the context of numerical verifications, the sphericity distribution within the particulate composite is taken to be Gaussian:

$$f(s) = N(\mu_s, \sigma_s) \tag{19}$$

where, μ_s and σ_s are the sphericity expectation and variance, respectively.

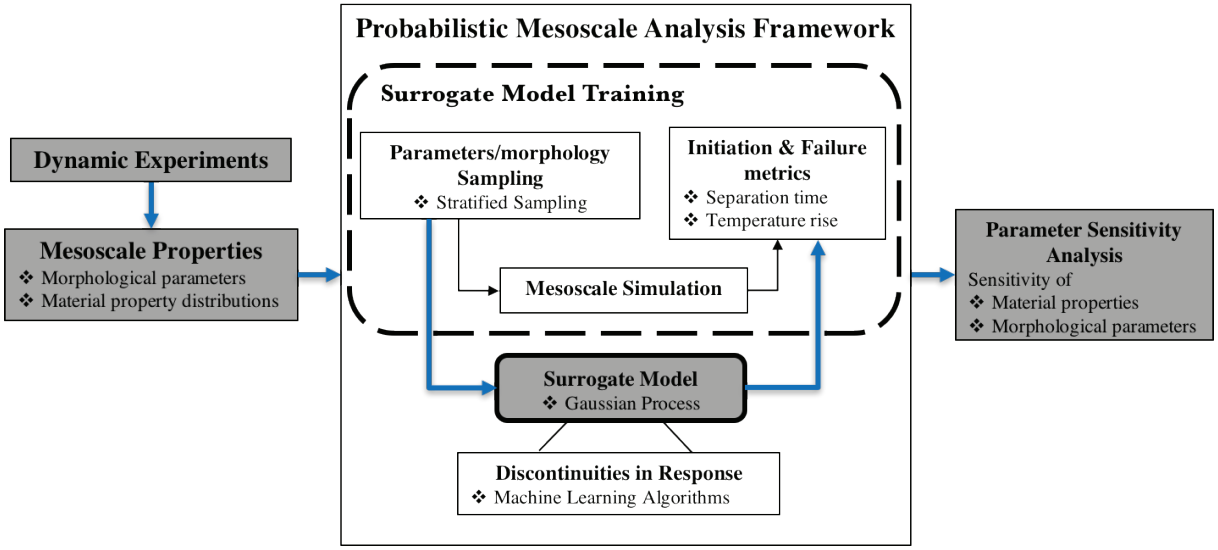

Figure 3: Overview of the proposed sensitivity analysis framework.

3 Sensitivity Analysis Framework

The proposed framework is established based the idea that parameter sensitivities of particulate materials should be quantified in a global sense (i.e., across the entire parameter space) to understand the role that each parameter plays on the corresponding failure mechanisms, and in the presence of discontinuous response surfaces under the applied loading. The proposed framework is schematically illustrated in Fig. 3.

The proposed framework relies on a parametric description of the mesoscale morphology as well as the constitutive response of the constituents (i.e., inclusion, binder, interface). The morphological and constitutive parameters are taken to be random variables. In order to perform sensitivity analysis, a set of samples is drawn to cover the entire subspace of physically plausible parameters. In order to avoid the necessity of performing direct mesoscale simulations for each sample point within the set, the proposed framework relies on adequately trained surrogate modeling (Gaussian Process, or GP) that relates the parameters to the response surface of a chosen mesoscale metric (e.g., interface separation, temperature rise, initiation). The sensitivity assessment is based on the Global Sensitivity Analysis (GSA) method. In GSA, the variance in the model output (i.e., mesoscale metric) results from the variance in the model input parameters (i.e., material parameters and the morphology), as well as the variance induced by the model input interactions. In this study, the contributions of the variance in each input to the variance in the output is characterized using the first order sensitivity and total effect indices. First order index represents the contribution to the output variance from the parameter itself, while total effect index also includes the interactions between the parameter and the other parameters.

(a) Stratified sampling.

(b) Uniform sampling

Figure 4: Comparison between stratified sampling and uniform sampling.

3.1 Stratified Sampling

The sampling of the parameter space is performed such that the following two requirements are satisfied: (1) The samples must cover the entire parameter space. This is in view of the fact that we seek to compute the sensitivity of the parameters across the entire parameter space, in contrast to local sensitivities. (2) The total number of samples must be as small as possible for computational efficiency, in view of the computational complexity of the mesoscale simulations. In the current study, the Stratified Sampling method [33] is employed. Stratified sampling ensures certain subspaces are not overrepresented or underrepresented. The idea of stratified sampling is to partition the parameter space to multiple non-overlapping subspaces, and to ensure that a set of samples from each subspace is drawn. Sampling within each subspace allows probing the local characteristics of the response function throughout the parameter space.

The benefit of employing the stratified sampling method is graphically illustrated in Fig. 4. In Fig. 4a, stratified sampling is applied to generate 100 randomly distributed samples in a two dimensional parameter space. The entire region is evenly divided as $10 \times 10 = 100$ subspaces with one sample per subspace. In Fig. 4b, uniform sampling was employed to draw 100 samples. The uniform sampling method fails to generate samples in 38 of the subspaces probed by stratified sampling, and fails to sample from large swaths of the parameter space. Alternative sampling approaches such as Sobol sequences [50] and other quasi Monte Carlo methods that uniformly sample the entire parameter space could also be employed with similar efficiency compared with the stratified sampling.

3.2 Gaussian Process Model

In view of the significant computational cost of performing mesoscale dynamic simulations, probing the entire parameter space within the context of sensitivity analysis through mesoscale simulations as a forward solver is computationally prohibitive. In this study, we employ Gaus-

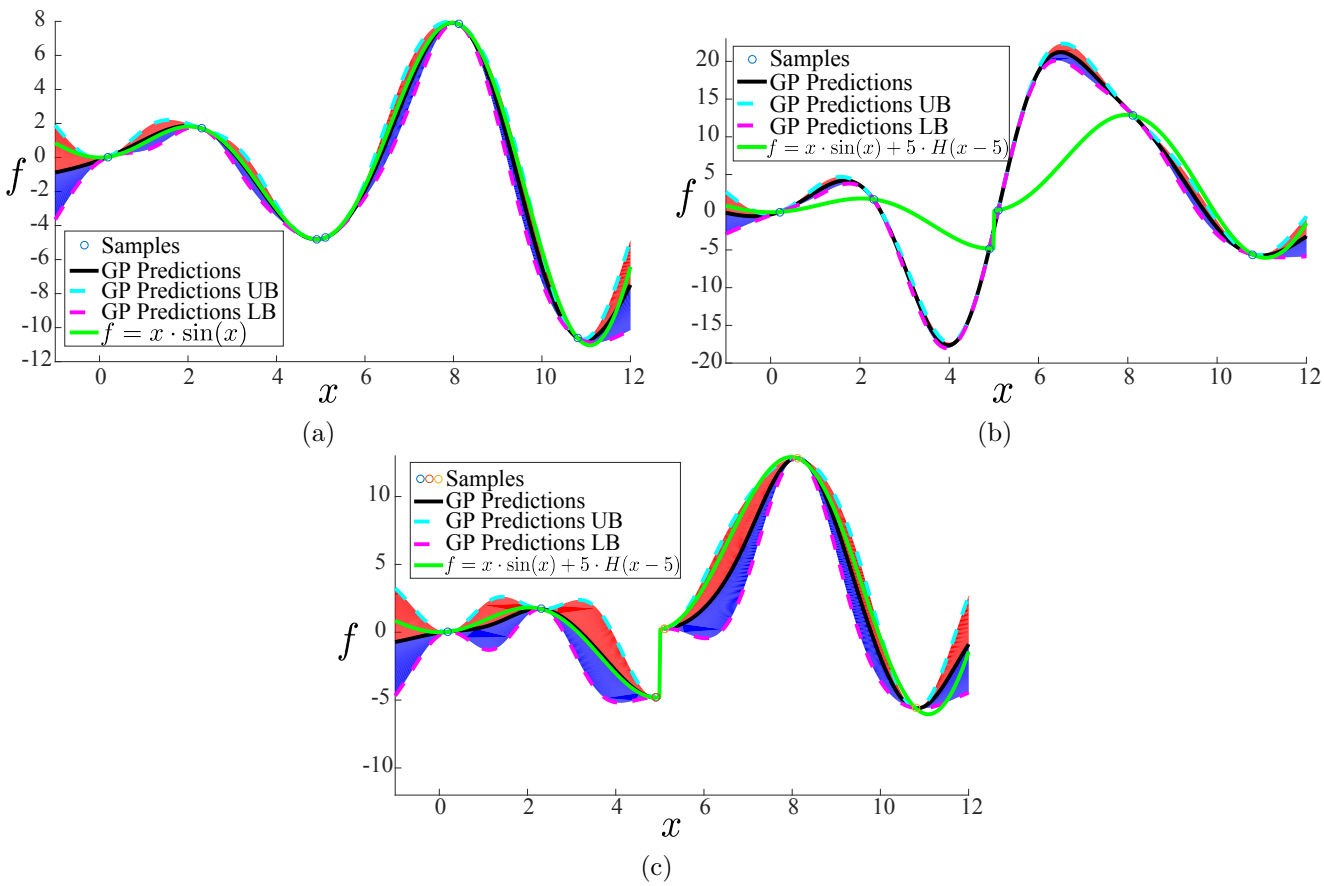

Figure 5: Example of GP model and discontinuity. Illustration of (a) a GP surrogate of function, $f = x \cdot \sin(x)$ trained with 6 training points; (b) a GP surrogate of function, $f = x \cdot \sin(x) + 5 \cdot H(x-5)$ trained with 6 samples; (c) two local GP surrogates of function, $f = x \cdot \sin(x) + 5 \cdot H(x-5)$ trained with 6 samples.

sian Process modeling as the surrogate forward simulator. In this approach, a small suite of mesoscale simulations are performed with randomly sampled parameters to generate discrete values of the response function, called training points. The training points are employed to construct the surrogate model, which is in turn employed to predict the response with randomly sampled prediction points.

Gaussian process (or Kriging) is a method of interpolation for which the interpolated values are modeled by a Gaussian process governed by prior covariance. The Gaussian process method is probabilistic, and it generates a distribution instead of a single prediction value at the prediction point. The variance of the prediction distribution is related to the proximity of the prediction point input (i.e., the parameter set that correspond to the prediction point) and the training point inputs as illustrated in Figure 5a.

The GP model is expressed in the following form:

$$G_p(\boldsymbol{u}) = \boldsymbol{h}(\boldsymbol{u})^T \cdot \boldsymbol{\beta} + Z(\boldsymbol{u}) \tag{20}$$

where $\boldsymbol{u} = (u^1, u^2, ..., u^d)$ denotes the vector of input parameters, each of which is a random variable, d denotes the number of parameters (i.e., the dimensionality of the problem), $\boldsymbol{h}$ is the trend of the model, $\boldsymbol{\beta}$ is the vector of trend coefficients, and Z is a stationary Gaussian process with zero mean. The trend of the model is taken to be up to second order polynomial regression model in this study, and higher order polynomial trend could be achieved via increasing the number of training samples.

The covariance between sample outputs is defined as

$$Cov[Z(\boldsymbol{a}), Z(\boldsymbol{b})] = \sigma_z^2 \cdot R(\boldsymbol{a}, \boldsymbol{b}) \tag{21}$$

where σ_z^2 is the process variance and $R(\cdot, \cdot)$ is the correlation function between two input points $\boldsymbol{a}$ and $\boldsymbol{b}$. Squared-exponential function, a commonly used correlation function is employed:

$$R(\boldsymbol{a}, \boldsymbol{b}) = \exp\left[-\sum_{i=1}^{d} \theta_i (a_i - b_i)^2\right] \tag{22}$$

where $\theta_i \in \boldsymbol{\theta} = (\theta_1, ..., \theta_d)$ is a parameter that indicates the correlation between the points within dimension i, a_i and b_i are the i_{th} components of $\boldsymbol{a}$ and $\boldsymbol{b}$, respectively.

The expectation value and variance of the GP model prediction distribution at input point $\boldsymbol{u}$ are expressed as:

$$\mu_G(\boldsymbol{u}) = \boldsymbol{h}(\boldsymbol{u}) \cdot \boldsymbol{\beta} + \boldsymbol{r}(\boldsymbol{u})^T \boldsymbol{R}^{-1}(\boldsymbol{g} - \boldsymbol{F}\boldsymbol{\beta}) \tag{23}$$

$$\sigma_G^2(\boldsymbol{u}) = \sigma_z^2(\boldsymbol{u}) - \begin{bmatrix} \boldsymbol{h}(\boldsymbol{u})^T & \boldsymbol{r}(\boldsymbol{u})^T \end{bmatrix} \begin{bmatrix} \boldsymbol{0} & \boldsymbol{F}^T \\ \boldsymbol{F} & \boldsymbol{R} \end{bmatrix}^{-1} \begin{bmatrix} \boldsymbol{h}(\boldsymbol{u}) \\ \boldsymbol{r}(\boldsymbol{u}) \end{bmatrix} \tag{24}$$

where $\boldsymbol{r}(\boldsymbol{u})$ is a vector containing the covariance between $\boldsymbol{u}$ and each of the n training points ($\boldsymbol{u}_1$, ..., $\boldsymbol{u}_n$), $\boldsymbol{R}$ is $n \times n$ matrix containing the correlation between each pair of training points, $\boldsymbol{g}$ is the vector of response outputs at each of the training points, and $\boldsymbol{F}$ is $n \times q$ matrix with rows $\boldsymbol{h}(\boldsymbol{u}_i)^T$, where q is the number of trend function terms for each row.

The process variance σ_z^2 and character parameter $\boldsymbol{\theta}$ are determined through maximum likelihood estimation. Taking the log of the probability of observing the response values $\boldsymbol{g}$ given the covariance matrix $\boldsymbol{R}$:

$$\log[p(\boldsymbol{g}|\boldsymbol{R})] = -\frac{1}{n} \log|\boldsymbol{R}| - \log\left(\hat{\sigma}_z^2\right) \tag{25}$$

where $|\boldsymbol{R}|$ indicates the determinant of $\boldsymbol{R}$, and $\hat{\sigma}_z^2$ is the optimal value of the variance given

an estimate of $\boldsymbol{\theta}$ and is defined by

$$\hat{\sigma}_z^2 = -\frac{1}{n}(\boldsymbol{g} - \boldsymbol{F}\boldsymbol{\beta})^T \boldsymbol{R}^{-1}(\boldsymbol{g} - \boldsymbol{F}\boldsymbol{\beta}) \tag{26}$$

Maximizing Eq. 25 gives the maximum likelihood estimate of $\boldsymbol{\theta}$, which in turn defines σ_z^2.

3.3 Discontinuities and Classifier

The response of particulate composites under dynamic loading conditions are marked by the presence of discontinuities induced by the discrete failure events that are functions of both material and morphological parameters. In contrast, the Gaussian Process models employing squared-exponential covariance functions or rational quadratic kernels exhibit significant errors when the response function is discontinuous [52]. Figure 5b illustrates the GP approximation of a function similar to that shown in Fig. 5a, but that contains a discontinuity. With the same training samples used in Fig. 5a, the GP model shown in Fig. 5b fails to accurately represent the discontinuous function.

In this manuscript, a piece-wise continuous GP model is proposed to account for the presence of discontinuities in the response functions. The piece-wise continuous GP model is built by employing the support vector machine (SVM) - a classification algorithm to solve the model selection problem.

Let $\Theta \subset \mathbb{R}^d$ denote the parameter space, which yields a discontinuous response function, $y(\boldsymbol{u})(\boldsymbol{u} \in \Theta)$. The response function is assumed to be continuous within q subdomains ($\Theta_a \subset \Theta; a = 1, ..., q$) separated by $(m-1)$ dimensional hyperplanes. The corresponding piecewise continuous GP approximation of the response function is expressed as:

$$GP(\boldsymbol{u}) = \sum_{a=1}^{q} N_a(\boldsymbol{u}) GP_a(\boldsymbol{u}) \tag{27}$$

in which GP_a denotes the continuous GP approximation valid within Θ_a; and N_a is a piecewise constant shape function:

$$N_a(\boldsymbol{u}) = \begin{cases} 1, & \text{if} \quad \boldsymbol{u} \in \Theta_a \\ 0, & \text{elsewhere} \end{cases} \tag{28}$$

Figure 5c illustrates a piece-wise continuous GP model in predicting the discontinuous function shown in Fig. 5b. The continuous parts on both sides of the discontinuity of the function are captured within the $\mu_G \pm 3\sigma_G$ interval by the two local surrogates.

The primary difficulty in the construction of the proposed surrogate model in Eq. 27 is that the parameter subdomains Θ_a are not known a-priori. We seek to identify the separator hyperplanes between the parameter subdomains based on a classification algorithm of the ma-

chine learning theory [26]. SVM is a discriminative classifier formally defined by a separating hyperplane/decision boundary [54]. For given set of input points $(\boldsymbol{u}_1, ..., \boldsymbol{u}_n)$ with their corresponding outputs $(\boldsymbol{y}_1, ..., \boldsymbol{y}_n)$, $\boldsymbol{\phi}$ is a mapping function from the input space to a hypothesis and potentially infinite-dimensional feature space [47] in which the inner product is $\langle \boldsymbol{\phi}(\boldsymbol{u}_i), \boldsymbol{\phi}(\boldsymbol{u}_j) \rangle$ such that the training set is linearly separable. The hyperplane is found through the following optimization problem:

$$\max_{\boldsymbol{w},b} \quad \min_i \left\{ \boldsymbol{y}_i \left[\langle \boldsymbol{w}, \boldsymbol{\phi}(\boldsymbol{u}_i) \rangle - b \right] \right\}$$

where $\langle \cdot, \cdot \rangle$ represents inner product, $\boldsymbol{w}$ is a vector, and b is a real number. The expression $(\langle \boldsymbol{w}, \boldsymbol{\phi}(\boldsymbol{u}_i) \rangle - b)$ is the distance between $\boldsymbol{u}_i$ and the decision boundary. The sign of $\boldsymbol{y}_i \{ \langle \boldsymbol{w}, \boldsymbol{\phi}(\boldsymbol{u}_i) \rangle - b \}$ is positive for the correct classifications and negative for the incorrect classifications. If all data sets are linearly separable, $\gamma = \min \left\{ \boldsymbol{y}_i \left[\langle \boldsymbol{w}, \boldsymbol{\phi}(\boldsymbol{u}_i) \rangle - b \right] \right\}$ is positive. It is proven in [8] that the decision function

$$f(\boldsymbol{u}) = \text{sign}(\langle \boldsymbol{w}, \boldsymbol{\phi}(\boldsymbol{u}) \rangle - b) \tag{29}$$

is equivalent to

$$f(\boldsymbol{u}) = \text{sign}(\sum_{i=1}^{n} \alpha_i \boldsymbol{y}_i \langle \boldsymbol{\phi}(\boldsymbol{u}_i), \boldsymbol{\phi}(\boldsymbol{u}) \rangle - b). \tag{30}$$

From this expression, it can be observed that only those points with non-zero α_i (called support vector) determine the hyperplane. The dot product between data point vectors, $\boldsymbol{\phi}(\boldsymbol{u}_i)$ and $\boldsymbol{\phi}(\boldsymbol{u}_j)$, is written as $K_{ij} = \langle \boldsymbol{\phi}(\boldsymbol{u}_i), \boldsymbol{\phi}(\boldsymbol{u}_j) \rangle$. Eq. 30 becomes:

$$f(\boldsymbol{u}) = \text{sign}(\sum_{i=1}^{n} \alpha_i \boldsymbol{y}_i \boldsymbol{K}(\boldsymbol{u}_i, \boldsymbol{u}_j) - b). \tag{31}$$

where $\boldsymbol{K}$ is the kernel matrix. In current study, quadratic kernel $K(\boldsymbol{u}_i, \boldsymbol{u}_j) = (\langle \boldsymbol{u}_i, \boldsymbol{u}_j \rangle + 1)^2$ is employed.

An additional and equally important problem is the identification of the number of discontinuities, q, within the parameter space. While not straightforward, those problems that exhibit unknown number of discontinuities could be addressed through cluster analysis in data mining, such as the elbow method [14], X-means clustering [35], Akaike information criterion [42], the silhouette method [41]. In the examples in this manuscript, the number of discontinuities are dictated by the physics of the problem and assumed to be known a-prior.

The performance of the classifier is assessed by k-folder cross-validation, which is a non-exhaustive cross-validation method [25] as illustrated in Fig. 6. The full set of input parameters is separated into k sets of equal size. An arbitrary subset is taken as the *validation set*, whereas the remaining $(k-1)$ sets are employed as *training sets*. The training sets are employed to

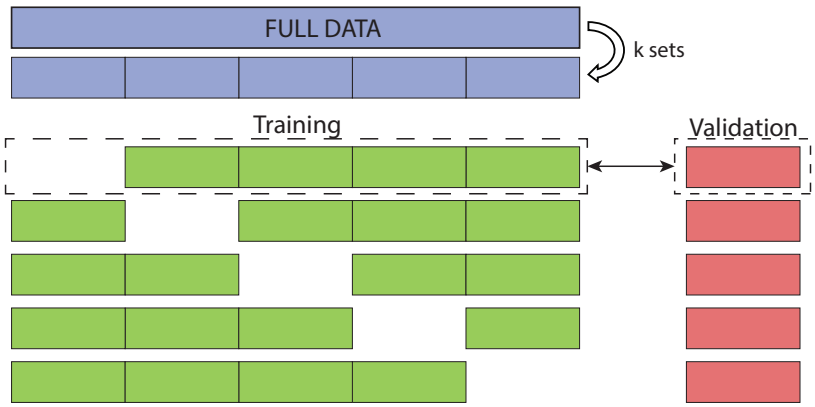

Figure 6: Cross-validation of the classification algorithm.

Table 1: Confusion matrix.

	Positive (Predict)	Negative (Predict)
Positive (Actual)	***True***	***False***
Negative (Actual)	***False***	***True***

construct the classifier. The validation set is then employed to assess whether the predicted classification (i.e., the associated parameter subdomain of each input, $\boldsymbol{u}_i$) is accurate. This process is repeated k times by assigning a different subset as the validation set.

Confusion matrix (i.e., error matrix) is produced by cross-validation to quantify the performance of a classifier (Table 1). Confusion matrix is a specific table layout that allows visualization of the performance of an algorithm. Each row of the confusion matrix represents the true class (i.e., the parameter subdomain), while each column of the confusion matrix represents the prediction of the classifier. For example, the $(i, j)_{\text{th}}$ element in the confusion matrix indicates the number or percentage of cases which belong to i_{th} parameter subdomain while predicted as j_{th} parameter subdomain. The diagonal terms represent the number or percentage of correct predictions of the classifier. For k-folder cross-validation, k confusion matrices are generated and summed to construct the overall confusion matrix.

3.4 Global Sensitivity Analysis

Among various sensitivity analysis methods, Global Sensitivity Analysis (GSA) has the ability to collect information from the entire input domain instead of local points, which makes the quantitive measurement of the sensitivity over the entire domain possible. The primary idea of GSA is to divide the uncertainty or variance of model output into different sources of uncertainty or variance of model inputs, and the contributions from different sources are

quantified by sensitivity indices.

The most sensitive parameter is identified through the GSA framework in both sense of self-contribution and parameter interactions, and insensitive parameters are set as constant in the view of computational complexity. In the view of multiple potential failure mechanisms, GSA provide the ability to understand the dominant mechanisms behind the complex input-output relationships over the input space, and eliminate the trivial influence from insensitive parameters. The parameter sensitivities obtained from GSA are parameter space dependent, considering that failure mechanisms are dominant at different parameter subspaces, and GSA focuses on the output uncertainty over the desired parameter space.

3.4.1 Decomposition of Variance

Arbitrary target function $y = f(\boldsymbol{u}) = f(u^1, ..., u^d)$ is decomposed as [49]

$$f(u^1, ..., u^d) = f_0 + [\sum_{i=1}^{d} \phi_i(u^i) + \sum_{i_1=1}^{d-1} \sum_{i_2=i_1+1}^{d} \phi_{i_1,i_2}(u^{i_1}, u^{i_2}) + ... + \phi_{1,2,...,d}(u^1, ..., u^d)] \tag{32}$$

where

$$\begin{cases} f_0 = \int f(\boldsymbol{u}) \prod_{i=1}^{d} [p_i(u^i) du^i] = E(y) & (33) \\ \phi_i(u^i) = \int f(\boldsymbol{u}) \prod_{j \neq i} [p_j(u^j) du^j] - f_0 = E_{u^{-i}}(y|u^i) - f_0 & (34) \\ \phi_{i_1,i_2}(u^{i_1}, u^{i_2}) = \int f(\boldsymbol{u}) \prod_{j \neq i_1, i_2} [p_j(u^j) du^j] - \phi_{i_1}(u^{i_1}) - \phi_{i_2}(u^{i_2}) - f_0 & (35) \end{cases}$$

with $p_i(u^i)$ the probably distribution function (PDF) of u^i, thus $\int f(\boldsymbol{u}) \prod_{j \neq i} [p_j(u^j) du^j]$ is $E_{u^i}(y|u^i)$ by definition. The constant f_0 is the expectation value of y. $\phi_i(u^i)$ represents the contribution of u_i to f only from itself, while $\phi_{i_1,i_2}(u^{i_1}, u^{i_2})$ represents the contribution from the interaction between u^{i_1} and u^{i_2} to f. The variance of y is obtained:

$$\mathrm{Var}(y) = \int [f(u^1, ..., u^d) - f_0]^2 \prod_{i=1}^{d} [p_i(u^i) du^i] \tag{36}$$

The parameters are taken to be independent (i.e., uncorrelated) random variables, which ensures the uniqueness of the the decompositions stated above [49].

3.4.2 Sensitivity Index

Sensitivity index is a measurement of the parameter sensitivity/importance to the model output variance. Sensitivity indices quantify the contribution of the parameter itself and the interaction between the parameter and other parameters across the entire input domain. The

first order index quantifies the contribution to output variance from the parameter itself, i.e., the first order terms in Eq. 32, while total effect index also includes the higher order terms in Eq. 32, i.e., the interactions between the parameter and the other parameters. Substituting Eq. 36 into Eq. 32:

$$1 = \sum_{i=1}^{d} S_i + \sum_{i_1=1}^{d-1} \sum_{i_2=i_1+1}^{d} S_{i_1 i_2} + ... + S_{1,2,...,d} \tag{37}$$

where the first order sensitivity index S_i is defined [49]:

$$S_i = \frac{\mathrm{Var}(\phi_i(u^i))}{\mathrm{Var}(y)} = \frac{\mathrm{Var}_{u^i}(E_{u^{-i}}(y|u^i))}{\mathrm{Var}(y)} \tag{38}$$

The notation u^{-i} represents all possible u^j for $j \neq i$. $\mathrm{Var}_{u^i}(E_{u^{-i}}(y|u^i))$ is the variance of the expectation of y given u^i . $E_{u^{-i}}(y|u^i)$ is computed by varying u^{-i} for a fixed u^i, whereas $\mathrm{Var}_{u^i}(E_{u^{-i}}(y|u^i))$ is calculated by varying u^i.

The total effect index, S_i^T, is expressed as:

$$S_i^T = 1 - \frac{\mathrm{Var}_{u^{-i}}(E_{u^i}(y|u^{-i}))}{\mathrm{Var}(y)} \tag{39}$$

where $E_{u^i}(y|u^{-i})$ is the expectation of y given u^{-i}. The total effect index S_i^T is the sum of first order index and corresponding higher order terms [18]:

$$S_i^T = S_i + \sum_{j}^{d} S_{ij} + \sum_{j_1=1}^{d-1} \sum_{j_2=j_1+1}^{d} S_{ij_1 j_2} + ... + S_{1,2,...,d} \tag{40}$$

where S_{ij} represents the interaction between u^i and u^j, $S_{ij_1 j_2}$ represents the interactions between u^i, u^{j_1} and u^{j_2}, $S_{1,2,...,d}$ is the interactions between all input parameters. The interaction terms in the total effect index is non-zero despite the fact that the parameter distributions are taken to be uncorrelated [28]. The numerical computation of sensitivity indices is performed using the Monte-Carlo based procedure proposed by Saltelli et al. [45]. The sum of total effect indices have the following property:

$$\sum_{i=1}^{d} S_i^T \geq 1 \tag{41}$$

This is due to the fact that the interaction between u^i and u^j is accounted for in both S_i^T and S_j^T.

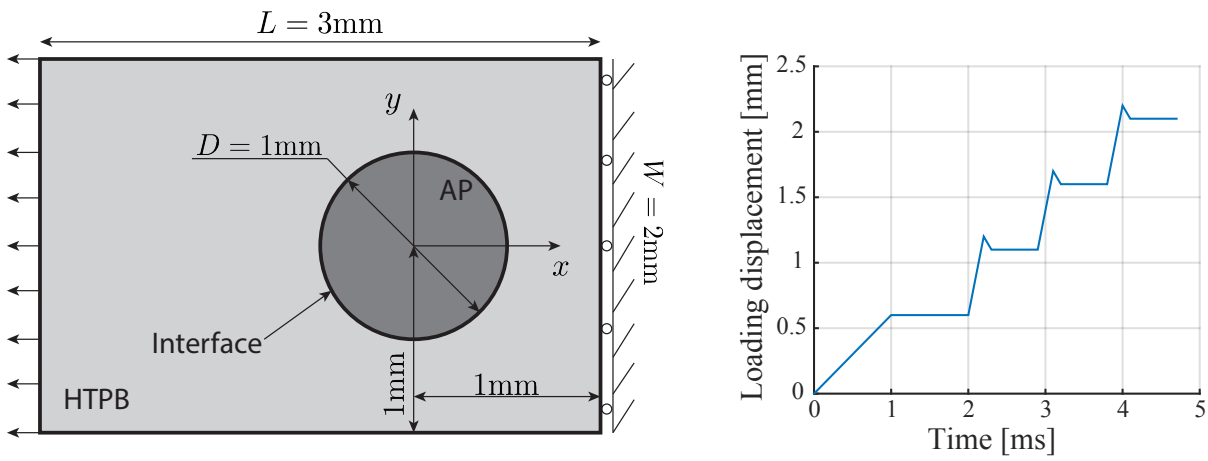

(a) (b)

Figure 7: Dynamic response of a single AP particle reinforced HTPB. (a) The geometry and boundary conditions; (b) the loading history.

4 Numerical Examples

The sensitivity analysis framework has been exercised to study two cases: (1) The dynamic response of a single AP particle embedded in HTPB binder. Particularly, the investigation focuses on the sensitivity of interfacial separation observed under impact loading to the parameters that describe the constitutive behavior of the binder and the interface. (2) The dynamic response of a multi-particle mesostructure subjected to ultrasonic vibration loading to study the size and morphology sensitivity of the temperature rise within the mesostructure.

4.1 Material Property Sensitivity

The dynamic response of energetic materials is sensitive to the particle/binder interface, since the interfacial separation, upon debonding, leads to temperature rise induced by frictional heating and dissipation within the binder. In the current numerical study, material properties, especially interfacial parameters, are investigated using the proposed framework.

4.1.1 Mesoscale Model

In this study, a fixed mesostructure that consists of a single AP particle embedded in the HTPB binder is considered. The mesoscale geometry and corresponding boundary conditions are illustrated in Fig. 7a. The 3 mm $\times$ 2 mm rectangular composite specimen includes a circular AP particle with a diameter of 1 mm. One edge of the specimen is fixed, while high rate impact loading is applied along the other edge. The displacement-controlled loading profile is shown in Fig. 7b, which consists of four step loadings. The loading rate in the first step is 600 mm/s, whereas the remaining three are applied at 3000 mm/s rate. The loading profile

Table 2: Binder and particle fixed parameters.

Parameter	ρ_h	ν_h	C_{V_h}	T_{ref}	A	B	E_{AP}	ρ_{AP}
Unit	g/mm^3		mJ/mm^{3}K	K			MPa	g/mm^3
Value	$0.95 \cdot 10^{-3}$	0.45	1.987	253	-15	102	$1.95 \cdot 10^4$	$1.95 \cdot 10^{-3}$
Parameter	$C_{V_{AP}}$	ν_{AP}	p_3	p_4	q_1	q_2	q_3	q_4
Unit	mJ/mm^{3}K		MPa	MPa	ms	ms	ms	ms
Value	2.121	0.3	25	13	$2 \cdot 10^{-5}$	$2 \cdot 10^{-4}$	$2 \cdot 10^{-3}$	$2 \cdot 10^{-2}$

is similar to a tensile Kolsky bar test that includes a quasi-static preload, followed by the applied load amplitude and multiple reflections. Under the applied loading, the AP particle is assumed to behave elastically. The HTPB binder undergoes viscoelastic deformation, and the interface progressively debonds based on the cohesive zone model described above. The response function of interest is the time to onset of interface separation defined as the time when the maximum separation reaches half of the particle diameter.

The AP particle Young's modulus and Poisson's ratio are obtained from [29]. The density ρ_{AP} is 1.95×10^{-3}, and the specific heat capacity per unit volume $C_{V_{AP}}$ is 2.121mJ/mm^{3}K [16].

Fifteen material parameters fully describe the thermo-mechanical deformation in the binder. The viscoelastic response is approximated using a four-component Prony Series model. The parameter set is split into two subsets. The first set consists of those parameters a-priori considered to be insensitive with respect to the response function, or are fixed. The density of the HTPB binder, ρ_h, is 0.95×10^{-3}g/mm^3. The Poisson's ratio of HTPB is taken to be 0.45, the same as that of Sylgard 184 [46, 53]. The specific heat capacity per unit volume, C_{V_h} is 1.987mJ/mm^{3}K [16]. The reference temperature T_{ref} and temperature shift factors A, B are kept consistent with Ref. [20]. The values of the fixed parameters are summarized in Table 2. The remainder of the parameters (i.e., the second set) are taken to be sensitive to the response function and employed as variables in the sensitivity study. The specific distributions of the parameters are unknown (due to lack of sufficient experiments to characterize the distributions). The parameters are therefore assumed to follow uniform distributions, which only require lower and upper bounds. The parameter ranges within the second set are identified based on experimental data and calibrated from stress-strain curves at different temperature and loading rates. Figure 8 shows the identification of the upper and lower bounds for the viscoelastic parameters (p_1, p_2, G_{h_∞}) by fitting bounds to the HTPB experimental stress-strain curves based on the data from Ref. [4]. The parameter ranges for the viscoelastic parameters employed in the sensitivity analysis are shown in Table 3.

Ten parameters describe the thermo-mechanical behavior and the progressive debonding along the particle-binder interface. Similar to the binder case, the parameter set is split into two subsets. The first set consists of those parameters a-priori considered to be insensitive

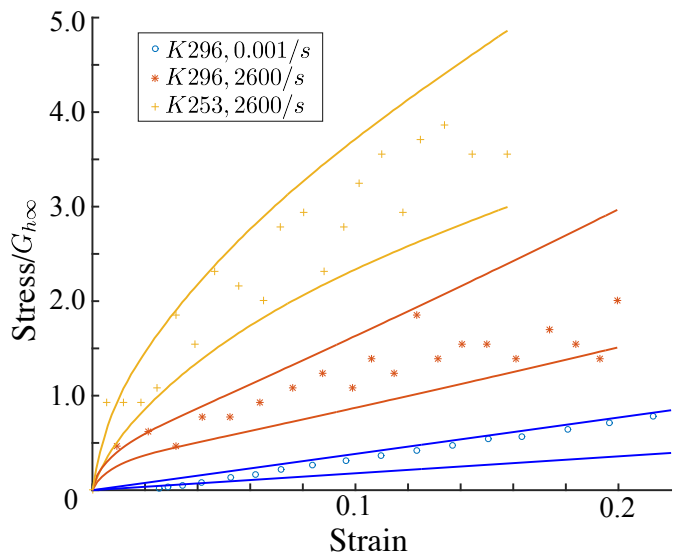

Figure 8: Prony series ranges calibration with experimental data.

Table 3: Parameter boundaries in material property sensitivity study.

Parameter	p_1	p_2	$G_{h\infty}$	$T_{\max}$	Δ_{cn}	Δ_{ct}	μ_0	w_{int}	ρ_{int}
Unit	MPa	MPa	MPa	MPa	mm	mm		mm	g/m^3
Upper bd	80	48	$1.95 \cdot 10^{-3}$	2.9	5	0.25	0.3	0.3	$3 \cdot 10^{-3}$
Lower bd	65	27	$0.95 \cdot 10^{-3}$	1.35	0.5	0.1	0.2	0.2	$2 \cdot 10^{-4}$

Table 4: Interfacial fixed parameters

Parameter	η_0	ϵ	β_s	$C_{V_{\text{int}}}$
Unit			MPa/mm	mJ/mm^{3}K
Value	0.014	10^{-5}	1900	2.054

with respect to the response function, or are fixed. The elastic limit η_0 is reported in [20]. The regularization parameter ϵ, which is introduced from the numerical efficiency point of view, is determined as 1×10^{-5} by a numerical parametric study in which the error caused by the regularization is not greater than 0.2% compared to the classical Coulomb law. The interfacial stiffness β_s is experimentally obtained by measuring the slope of the stress-strain curve [20]. The interfacial heat capacity $C_{V_{\text{int}}}$ is taken as the average of the two material phases (AP and HTPB), i.e., $C_{V_{\text{int}}} = 2.054\text{mJ/mm}^3\text{K}$. The values of the fixed parameters are summarized in Table 4. The remainder of the parameters are taken to be sensitive to the response function and employed as variables in the sensitivity study. The maximum traction $T_{\max}$, the critical normal separation Δ_{cn}, the critical tangential separation Δ_{ct}, the interfacial width w_{int}, the interfacial density ρ_{int}, and the friction coefficient μ_0 are included as variables in the sensitivity study. Parameter ranges of the cohesive zone model are selected based on the properties of the PBXs investigated in Refs. [1, 15, 20, 36, 51, 63] and listed in Table 3.

Table 5: Overall accuracies of classifiers

Classifier	Linear SVM	Simple Tree	Coarse KNN[1]	LD[2]
Accuracy	94.4%	81.4%	95.3%	90.4%
Prediction Speed [obj/s[4]]	~ 28000	~ 96000	~ 33000	~ 72000
Classifier	Quadratic SVM	Medium Tree	Medium KNN	QD[3]
Accuracy	98.2%	96.6%	96.6%	91.0%
Prediction Speed [obj/s]	~ 25000	~ 120000	~ 57000	~ 52000

[1] k-Nearest Neighbor
[2] LD represents linear discriminant
[3] QD represents quadratic discriminant
[4] obj/s represents objective (or number of function evaluations) per second

In summary, three binder parameters (i.e., p_1, p_2 and G_{h_∞}) and six interfacial parameters (i.e., $T_{\max}$, Δ_{cn}, Δ_{ct}, w_{int}, ρ_{int}, and μ_0) for a total of nine parameters are included in the current sensitivity study.

4.1.2 Local GP Models and Classifier

Under the applied step-wise loading, interface separation (as a function of material parameters) tends to cluster near the load steps. This results in a multi-modal distribution of time-to-separation as further discussed below. In order to accurately approximate this behavior using surrogate modeling, we employed the piecewise continuous GP model (Eq. 27). The classifier SVM provides higher accuracy than some of the other classifiers (e.g. decision tree, k-Nearest Neighbor Classifier, discriminant analysis) at the cost of added computational complexity, as shown in Table 5.

A five-part GP model has been constructed to predict the sensitivity of the nine material parameters on the failure behavior of the composite. The five-part model corresponds to the parameter subspaces that result in failure near the four step loads, in addition to the subspace that result in no interface separation.

In Fig. 9, Von Mises stress contours are plotted from four representative simulations at the state of interface failure (i.e., separation time). The contour plots indicates a change in interface separation characteristics in addition to separation time as a function of constituent parameters. The proposed five-part GP model is trained by a suite of training points that are obtained through the dynamic analysis of the mesostructure using the finite element method with randomly sampled parameters using the stratified sampling method. The accuracy of the GP model has been assessed by verifying the convergence as a function of the number of training points, and the number of prediction points, as well as by verifying the accuracy of subspace classification through the confusion matrix.

Figure 10a illustrates the convergence of the GP model as a function of the number of

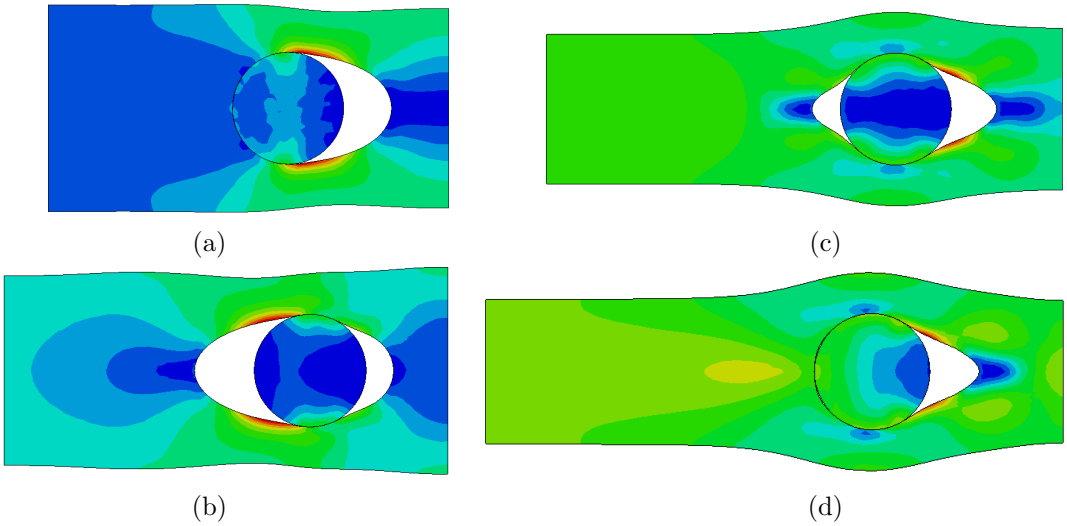

Figure 9: Von Mises stress contours of single particle system failure at (a) $t = 1.04$ ms; (b) $t = 2.12$ ms; (c) $t = 3.08$ ms; (d) $t = 3.932$ ms.

training points employed. The figure shows the prediction of time-to-separation PDFs based on three piecewise continuous GP models trained by 256, 512, 5120 mesoscale simulations. The PDFs were generated using 20 million prediction points for all three models. While the model trained by 256 training points demonstrates significant discrepancy, the models trained by 512 and 5120 indicates close match. In the remainder of the numerical study, we employ the GP model trained by 5120 training points. Figure 10b shows the convergence of the GP model predictions as a function of the number of prediction points. The figure demonstrates that the GP model predictions converge after a relatively large number of prediction points are employed ($\sim$2 million). It is important to note that the figure illustrates those prediction points that lead to separation. The distributions with low number of prediction points demonstrates a higher ratio of cases in which separation does not initiate.

The performance of the SVM classifier is assessed by the confusion matrix which is generated by a 10-folder cross-validation as shown in Fig. 11.

In Fig. 11b, all the diagonal terms (indicating correct classification) are greater than 90%, which indicates that the classifier correctly predicts the appropriate parameter subspace with over 90% accuracy. Increasing accuracy is observed as the number of training points increases from 512 (Fig. 11a) to 5120 (Fig. 11b) employing quadratic SVM classifier.

4.1.3 Global Sensitivity Analysis

The parameter boundaries which define the parameter space of interest are provided in Table 3. The most sensitive parameters using the first order sensitivity and total effect sensitivity are identified according to the indices of each parameter.

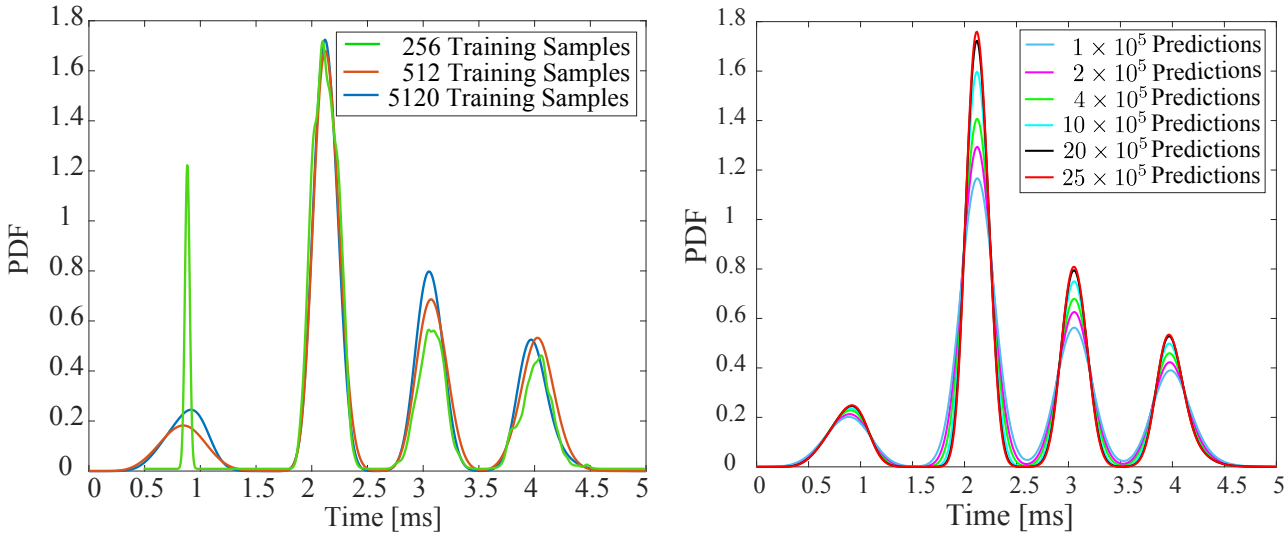

(a) (b)

Figure 10: Convergence study of GP model with respect to (a) the number of training samples with prediction distributions generated with 2 million samples; and (b) the number of prediction points with the surrogate trained with 5120 samples.

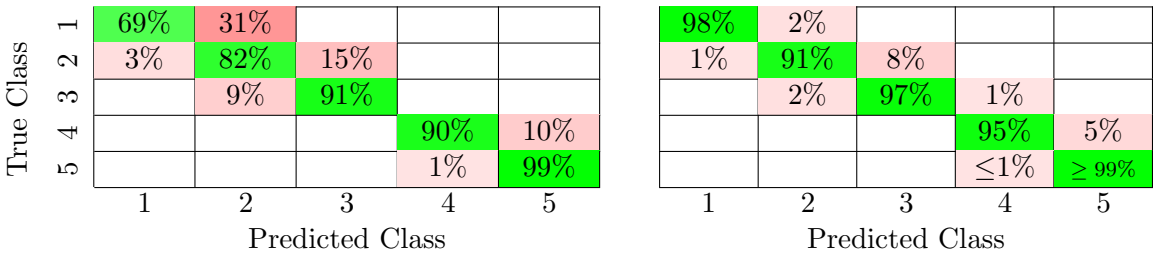

(a) (b)

Figure 11: Confusion matrix. Class i: separation initiation near the ith step load (i $\leq$ 4). Class 5: no separation ovserved. (a) confusion matrix trained with 512 samples. (b) confusion matrix trained with 5120 samples.

Sensitivity indices, the quantitive representation of parameter contribution to interfacial separation, are shown in Fig. 12a. Interface strength $T_{\max}$ is the dominant parameter based on self-contribution as well as parameter interactions. The critical normal separation and G_{h_∞} are also identified as significant uncertainty sources in this system. The higher order interactions between multiple factors significantly increase the sensitivities of Δ_{cn} and G_{h_∞}. Compared to critical normal separation, the critical tangent separation is an insensitive parameter, despite the presence of shear stress concentration as reported in [20]. Prony Series and other interfacial parameters are observed to be insensitive factors as well. Figure 12b demonstrates the convergence of the sensitivity measures as a function of the number of prediction samples. The figure indicates convergence with approximately 20 million prediction samples.

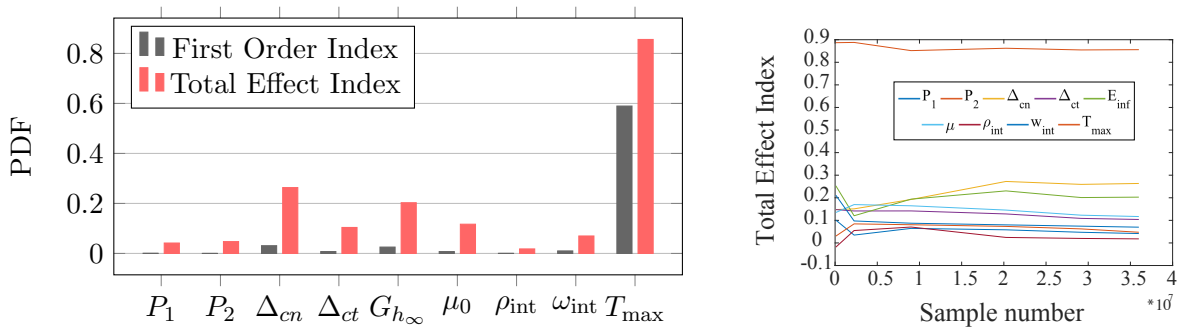

(a) Sensitivity indices for material properties.

(b) Convergence of S_i^T.

Figure 12: Convergence study of GP model with respect to (a) the number of training samples with prediction distributions generated with 20 million samples; and (b) the number of prediction points with the surrogate trained with 5120 samples.

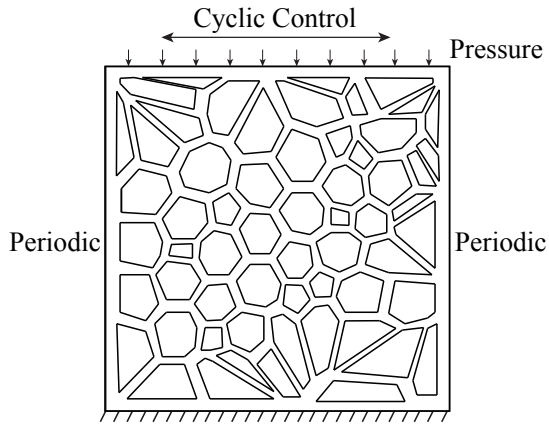

Figure 13: Geometry and loading conditions.

4.2 Mesoscale Geometry Sensitivity

The local temperature rise ("hot spots") induced by local mesostructure response in multiple particle systems under dynamic loading is of interest, since hot spots are among the failure mechanisms in energetic materials. In the current numerical study, the mesoscale geometry characteristics of the particulate composite, for example, particle size and particle shape, are parameterized and investigated using the GSA framework.

4.2.1 Mesoscale Model

In this numerical study, the thermo-mechanical dynamic behavior of a multiple particle AP-HTPB composite specimen under ultrasonic vibration loading is investigated to assess the contribution of geometric parameters on the temperature rise in the specimen. The specimen is idealized as a 3 mm $\times$ 3 mm rectangle with multiple polygons (idealized particles) embedded as shown in Fig. 13. The bottom edge is fixed, and the periodic boundary condition is applied

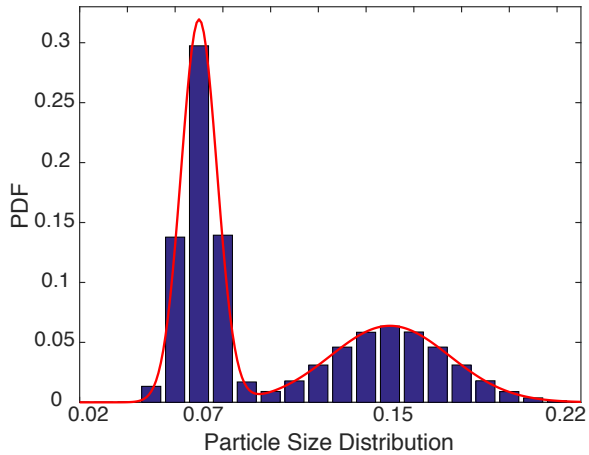

Figure 14: Illustration of particle size distribution. Above PDF is subjected to a bimodal distribution with $\mu_1 = 0.15$ mm^2, $\mu_2 = 0.07$ mm^2, $\sigma_1 = 0.025$ mm^2, $\sigma_2 = 0.0075$ mm^2, $w_1 = 0.6$.

on the side edges. Static pressure, $p = 200$ KPa, and a harmonic loading, $d_h = A_v \cdot \sin(2\pi f \cdot t)$, are both applied on the top surface as external excitation. $A_v = 0.03$ mm is the loading amplitude, and $f = 40$ kHz is the ultrasonic frequency.

Mesoscale geometry of particulate composites is defined by the particle size distribution, the particle shape distribution, and the particle area fraction. The mesoscale geometry of AP-HTPB system is assumed to be controlled by the above parameterized distribution parameters and constructed by Neper [37], a polycrystalline microstructure generation software. The geometry of the particles obtained from Neper is adjusted to reach the desired area fraction, and the binder model is applied on the gap between the AP particles to include the interaction of particles through the soft HTPB binder. The cohesive zone element is inserted between particle and binder to reproduce the interfacial behavior.

In the context of numerical verifications, a bimodal particle size distribution is assumed [2]:

$$f(A) = w_1 \cdot N(\mu_1, \sigma_1) + (1 - w_1) \cdot N(\mu_2, \sigma_2) \tag{42}$$

where w_1 is the weight for the first mode. μ_1 and σ_1 are the mean and variance of the normal distribution of the first mode. μ_2 and σ_2 are the mean and variance of the second mode, as illustrated in Fig. 14.

Sensitivities of five mesostructure parameters that define the mesoscale geometry (particle size distribution means μ_1, μ_2, bimodal weight ω_1, particle sphericity distribution mean μ_s, and area fraction η) are investigated. Similar to the previous example, uniform distribution is assumed for each parameter. The values of parameter ranges are selected according to experimental and numerical energetic mesostructure data available in the literature [1, 56,

Table 6: Parameters boundary in mesoscale geometry sensitivity study.

Parameter	μ_1	μ_2	μ_s	ω_1	η
Unit	mm^2	mm^2			
Upper bd	0.2	0.07	0.9	1.0	0.9
Lower bd	0.1	0.04	0.8	0.5	0.7

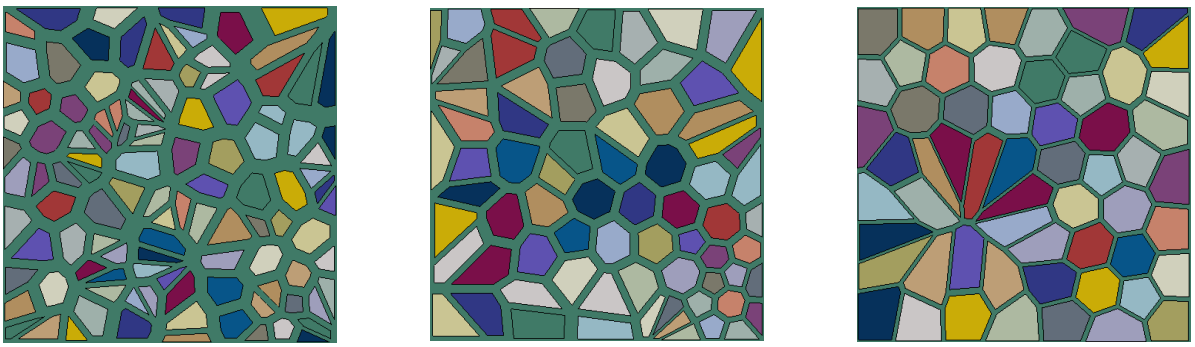

(a) (b) (c)

Figure 15: Examples of mesoscale geometry with size and shape parameters at (a) lower boundaries; (b) mean values; (c) upper boundaries in Table 6.

Table 7: Fixed parameters in mesoscale geometry sensitivity study.

Parameter	$T_{\max}$	Δ_{cn}	Δ_{ct}	μ_0	w_{int}	ρ_{int}	$G_{h\infty}$
Unit	MPa	mm	mm		mm	g/m^3	MPa
Value	2.91	0.11	0.264	0.2	10^{-3}	$1.45 \cdot 10^{-3}$	2.5

27, 17, 9, 30, 10, 61, 21] and listed in Table 6. Variations of these five parameters directly influence the mesoscale geometry, and three examples in Fig. 15 are employed to demonstrate the influence of the parameters on the resulting mesoscale geometry. The variance of the first mode and second mode, σ_1 and σ_2 are kept as 0.025 mm and 0.0075, respectively. The variance of sphericity σ_s is selected as 0.15.

Material parameters except the Prony Series (i.e., AP particle properties, interface parameters) set in the previous example are used in the current study as well. Six interfacial parameters and the steady-state shear modulus employed before are assumed to be constants and shown in Table 7. Six pairs of Prony Series are employed to represent the viscoelastic behavior of HTPB binder and calibrated from experimental data [4]. The calibrated stress-strain curves using six pairs of Prony Series are plotted in Fig. 16, and corresponding moduli and relaxation times are shown in Table 8.

In order to ensure that the element discretization is sufficient to capture the dynamic response, a mesh convergence study with respect to the target response functions (i.e., temperature) is performed. For a representative case as shown in Fig. 17a, the specimen is deformed

Table 8: Calibrated six pairs of prony series.

Parameter	p_1	p_2	p_3	p_4	p_5	p_6
Value	33	30	25	13	8	3
Parameter	q_1	q_2	q_3	q_4	q_5	q_6
Value	$1.04 \cdot 10^{-7}$	$2.1 \cdot 10^{-5}$	$1.66 \cdot 10^{-3}$	$1.05 \cdot 10^{-2}$	$5 \cdot 10^{-2}$	$2.1 \cdot 10^{-1}$

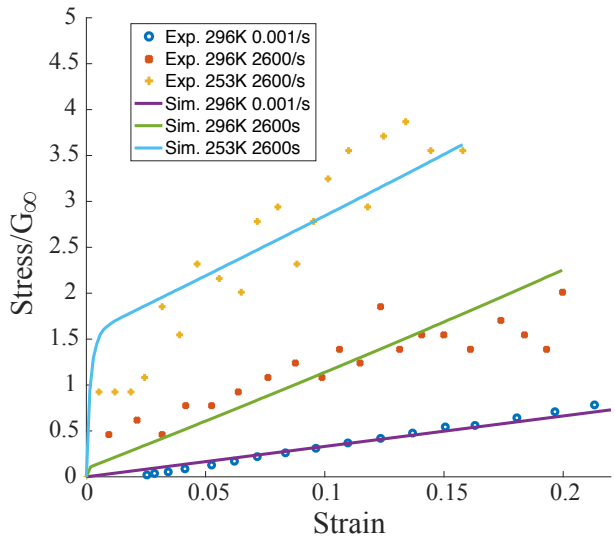

Figure 16: Prony Series Calibration

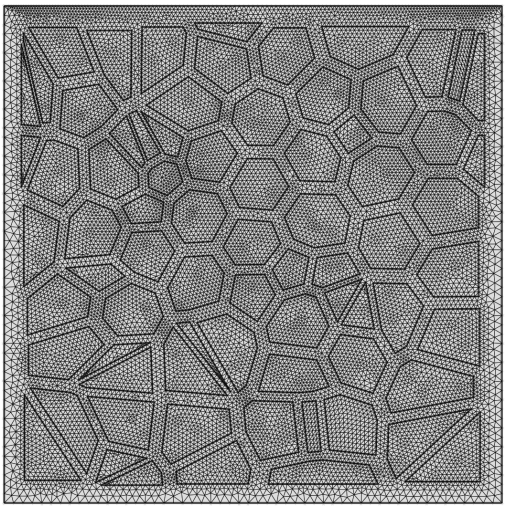

(a)

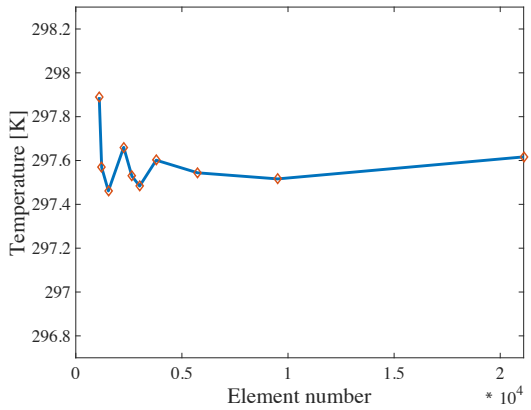

(b)

Figure 17: Mesh convergence study of the representative case. (a) Mesh of the representative mesostructure with 21104 elements; (b) Element number convergence.

under ultrasonic loading for 1 ms. The maximum temperature after 1 ms as the response function of the mesh convergence study changes with mesh refinement and its convergence trend is plotted in Fig. 17b. When the number of elements reaches to around 6,000, the maximum

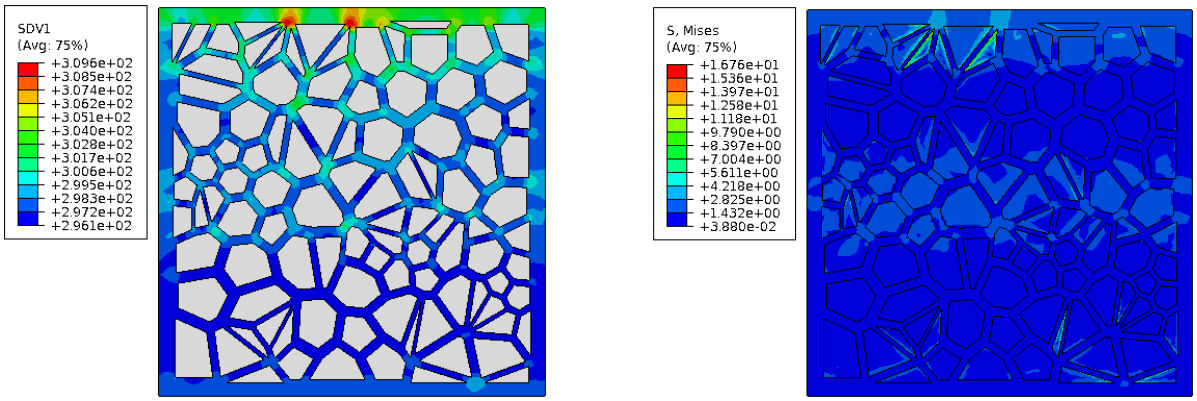

(a) (b)

Figure 18: Example of mesoscale FE simulations of multiple particle systems. (a) Temperature contour of binder at $t = 10$ ms; (b) Von Mises stress contour at $t = 10$ ms.

temperature in the specimen after the ultrasonic excitation is loaded for 1 ms is stable. All forward mesoscale simulations employ a level of discretization similar to the converged model described in this study.

4.2.2 GP Surrogate Model

Although high temperature may exist at multiple local sites within the mesostructure, as shown in Fig. 18, the maximum temperature within the specimen is chosen as the response function. A GP surrogate is trained to substitute the complex mesoscale FE simulation (Fig. 18). The convergence with respect to the number of training samples is guaranteed by constructing four GP models with 32, 64, 96, and 128 mesoscale simulations as training points. Four prediction distributions constructed with GP models trained by different sample sizes are compared and the convergence is observed, as shown in Fig. 19a. The PDFs were generated using forty million prediction points for all four models. These four distributions are not identical, but three of them (produced by GP models trained with 64, 96, 128 samples) are similar and can be regarded as converging. In current study, the GP model with 64 training simulations is employed.

Similar to the previous study, the convergence of prediction distributions should be guaranteed before checking the convergence of the number of training samples. Forty million prediction points are necessary to generate the converged prediction distribution, as shown in Fig. 19b.

4.2.3 Global Sensitivity Analysis

Five mesoscale geometry parameters that represent the mesostructure characteristics are investigated through the proposed sensitivity analysis framework. Sensitivity indices quantifying

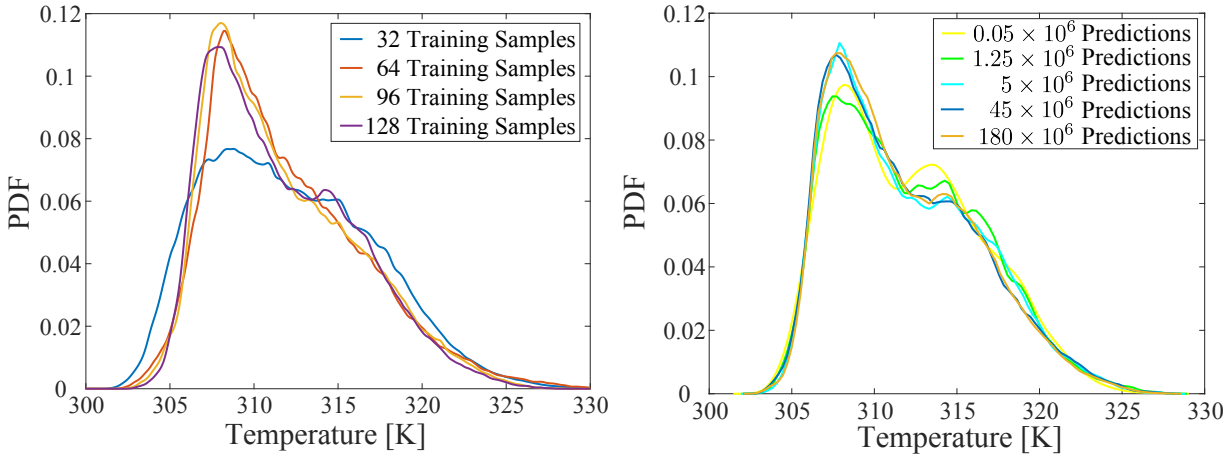

(a) (b)

Figure 19: Convergence study of GP model with respect to (a) the number of training samples with prediction distributions generated with 40 million samples; (b) the number of prediction points with the surrogate trained with 128 samples.

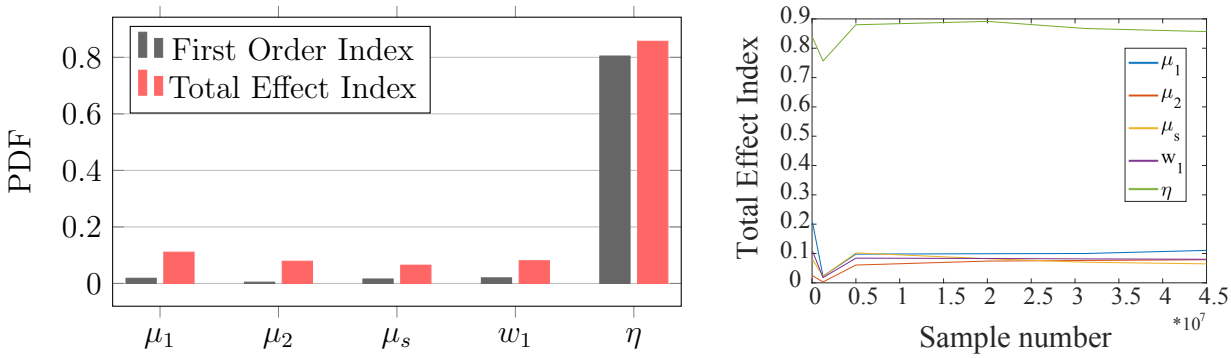

(a) Sensitivity indices in geometry sensitivity study. (b) Convergence of S_i^T.

Figure 20: Convergence study of GP model with respect to (a) the number of training samples with prediction distributions generated with 45 million samples; and (b) the number of prediction points with the surrogate trained with 5120 samples.

contributions from parameters and interactions are obtained, and the dominant parameter is identified.

The sensitivity indices obtained from the GSA framework are shown in the Fig. 20a. The results indicate that the area fraction is the dominant parameter that contributes to the temperature rise in the dynamic simulations. The dominant effect of area fraction is primarily due to the higher stress concentrations observed in particles in close proximity to one another. It is interesting to note that the sphericity parameter appears to have little influence on the localized heating characteristics. This result is surprising since higher stresses are expected near low sphericity particles. This result is attributed to the fact that the parameter range for sphericity is kept relatively narrow in the sensitivity study. This is to avoid the need to employ

very fine discretization near narrow edges of the particles. From the physical perspective, it can be speculated that very fine asperities of the particles break off at the early stages of the dynamic loading, rounding the particle geometries prior to the onset of localized heating. Comparing the total and first order sensitivity indices, the contributions of the parameter interactions appear to be significant for particle mean sizes, the weight and sphericity expectation parameters. The larger particle mean size exhibits larger influence than the smaller particle mean size to the maximum temperature within the particulate composite. Figure 20b demonstrates the convergence of the sensitivity measures as a function of the number of prediction samples. The figure indicates convergence with approximately 20 million prediction samples.

5 Conclusion

This manuscript presented a new global sensitivity analysis framework for problems that exhibit discontinuous response functions. The proposed approach has been applied to investigate the role of material and morphological properties of particulate energetic composite materials subjected to dynamic loading conditions. In particular, the following conclusions are drawn: (1) the piece-wise continuous GP model with SVM classier to characterize the continuous subdomains provide a computationally accurate and efficient approach to characterize sensitivities in the presence of response function discontinuities; (2) Interface strength and particle volume fraction are found to be the most influential parameters in the loading regime and mesoscale morphologies investigated in this study.

Acknowledgments

The authors gratefully acknowledge the financial support from the Air Force Office of Scientific Research, Dynamic materials and Interactions program (Grant No.: FA9550- 15-1-0202, Program Manager: Dr. Martin Schmidt).

References

[1] A. Barua and M. Zhou. A lagrangian framework for analyzing microstructural level response of polymer-bonded explosives. *Modelling and Simulation in Materials Science and Engineering*, 19(5):055001, 2011.

[2] A. Barua, S. Kim, Y. Horie, and M. Zhou. Ignition criterion for heterogeneous energetic materials based on hotspot size-temperature threshold. *Journal of Applied Physics*, 113 (6):064906, 2013.

[3] F. P. Bowden and A. D. Yoffe. *Initiation and growth of explosion in liquids and solids.* CUP Archive, 1952.

[4] C. M. Cady, W. R. Blumenthal, G. T. Gray, and D. J. Idar. Mechanical properties of plastic-bonded explosive binder materials as a function of strain-rate and temperature. *Polymer Engineering & Science*, 46(6):812–819, 2006.

[5] S. Chatterjee and A. S. Hadi. *Sensitivity analysis in linear regression*, volume 327. John Wiley & Sons, 2009.

[6] H. Christopher Frey and S. R. Patil. Identification and review of sensitivity analysis methods. *Risk Analysis*, 22(3):553–578, 2002.

[7] C. Cortes and V. Vapnik. Support-vector networks. *Machine Learning*, 20(3):273–297, 1995.

[8] N. Cristianini and J. S.-Taylor. *An introduction to support vector machines.* Cambridge University Press Cambridge, 2000.

[9] H. Czerski and W. G. Proud. Relationship between the morphology of granular cyclotrimethylene-trinitramine and its shock sensitivity. *Journal of Applied Physics*, 102 (11):113515, 2007.

[10] H. Czerski and W. G. Proud. Relationship between the morphology of granular cyclotrimethylene-trinitramine and its shock sensitivity. *Journal of Applied Physics*, 102 (11):113515, 2007.

[11] L. Delannay, P. J. Jacques, and S. R. Kalidindi. Finite element modeling of crystal plasticity with grains shaped as truncated octahedrons. *International Journal of Plasticity*, 22(10):1879–1898, 2006.

[12] M. Elices, G. V. Guinea, J. Gomez, and J. Planas. The cohesive zone model: advantages, limitations and challenges. *Engineering Fracture Mechanics*, 69(2):137–163, 2002.

[13] J. E. Field. Hot spot ignition mechanisms for explosives. *Accounts of Chemical Research*, 25(11):489–496, 1992.

[14] G. Hackeling. *Mastering Machine Learning with scikit-learn*. Packt Publishing Ltd, 2014.

[15] B. Han, Y. Ju, and C. Zhou. Simulation of crack propagation in HTPB propellant using cohesive zone model. *Engineering Failure Analysis*, 26:304–317, 2012.

[16] D. M. Hanson-Parr and T. P. Parr. Thermal properties measurements of solid rocket propellant oxidizers and binder materials as a function of temperature. *Journal of Energetic Materials*, 17(1):1–48, 1999.

[17] E. B. Herbold, V. F. Nesterenko, D. J. Benson, J. Cai, K. S. Vecchio, F. Jiang, J. W. Addiss, S. M. Walley, and W. G. Proud. Particle size effect on strength, failure, and shock behavior in polytetrafluoroethylene-al-w granular composite materials. *Journal of Applied Physics*, 104(10):103903, 2008.

[18] T. Homma and A. Saltelli. Importance measures in global sensitivity analysis of nonlinear models. *Reliability Engineering & System Safety*, 52(1):1–17, 1996.

[19] S.-W. Hsiao and N. Kikuchi. Numerical analysis and optimal design of composite thermoforming process. *Computer Methods in Applied Mechanics and Engineering*, 177(1-2): 1–34, 1999.

[20] R. Hu, C. Prakash, V. Tomar, M. Harr, I. E. Gunduz, and C. Oskay. Experimentally-validated mesoscale modeling of the coupled mechanical–thermal response of AP-HTPB energetic material under dynamic loading. *International Journal of Fracture*, 203(1): 277–298, 2017.

[21] R. J. Hudson, M. Moniruzzaman, and P. P. Gill. Investigation of crystal morphology and shock sensitivity of cyclotrimethylenetrinitramine suspension by rheology. *Propellants, Explosives, Pyrotechnics*, 40(2):233–237, 2015.

[22] R. L. Iman and J. C. Helton. An investigation of uncertainty and sensitivity analysis techniques for computer models. *Risk Analysis*, 8(1):71–90, 1988.

[23] M. Inoue and I. Hirasawa. The relationship between crystal morphology and XRD peak intensity on $CaSO_4{\cdot}2H_2O$. *Journal of Crystal Growth*, 380:169 – 175, 2013.

[24] T. L. Jackson, D. E. Hooks, and J. Buckmaster. Modeling the microstructure of energetic materials with realistic constituent morphology. *Propellants, Explosives, Pyrotechnics*, 36 (3):252–258, 2011.

[25] R. Kohavi et al. A study of cross-validation and bootstrap for accuracy estimation and model selection. In *Ijcai*, volume 14, pages 1137–1145. Stanford, CA, 1995.

[26] S. B. Kotsiantis, I. Zaharakis, and P. Pintelas. Supervised machine learning: A review of classification techniques. *Informatica*, 31:249-268, 2007.

[27] N. V. Kozyrev, B. V. Larionov, and G. V. Sakovich. Influence of HMX particle size on the synthesis of nanodiamonds in detonation waves. *Combustion, Explosion, and Shock Waves*, 44(2):193–197, 2008.

[28] G. Li, H. Rabitz, P. E. Yelvington, O. O. Oluwole, F. Bacon, C. E. Kolb, and J. Schoendorf. Global sensitivity analysis for systems with independent and/or correlated inputs. *The Journal of Physical Chemistry A*, 114(19):6022–6032, 2010.

[29] D. A. Lucca, M. J. Klopfstein, O. R. Mejia, L. Rossettini, and L. T. DeLuca. Investigation of ammonium perchlorate by nanoindentation. *Materials Science and Technology*, 22(4): 396–401, 2006.

[30] J. K. Miller, J. O. Mares, I. E. Gunduz, S. F. Son, and J. F. Rhoads. The impact of crystal morphology on the thermal responses of ultrasonically-excited energetic materials. *Journal of Applied Physics*, 119(2):024903, 2016.

[31] M. D. Morris. Factorial sampling plans for preliminary computational experiments. *Technometrics*, 33(2):161–174, 1991.

[32] E. J. Mulrow. *The visual display of quantitative information.* Taylor & Francis, 2002.

[33] J. Neyman. On the two different aspects of the representative method: the method of stratified sampling and the method of purposive selection. *Journal of the Royal Statistical Society*, 97(4):558–625, 1934.

[34] R. Panchadhara and K. A. Gonthier. Mesoscale analysis of volumetric and surface dissipation in granular explosive induced by uniaxial deformation waves. *Shock Waves*, 21(1): 43–61, 2011.

[35] D. Pelleg and A. W. Moore. X-means: Extending k-means with efficient estimation of the number of clusters. In *ICML*, volume 1, pages 727–734, 2000.

[36] C. Prakash, D. Verma, M. Exner, E. Gunduz, and V. Tomar. Strain rate dependent failure of interfaces examined via nanoimpact experiments. In *Challenges in Mechanics of Time Dependent Materials, Volume 2*, pages 93–102. Springer, 2017.

[37] R. Quey, P. R. Dawson, and F. Barbe. Large-scale 3D random polycrystals for the finite element method: Generation, meshing and remeshing. *Computer Methods in Applied Mechanics and Engineering*, 200(17):1729–1745, 2011.

[38] H. Rabitz, M. Kramer, and D. Dacol. Sensitivity analysis in chemical kinetics. *Annual Review of Physical Chemistry*, 34(1):419–461, 1983.

[39] P. J. Rae, H. T. Goldrein, S. J. P. Palmer, J. E. Field, and A. L. Lewis. Quasi–static studies of the deformation and failure of β–HMX based polymer bonded explosives. *Proceedings of the Royal Society of London A: Mathematical, Physical and Engineering Sciences*, 458 (2019):743–762, 2002.

[40] E. Rohan and B. Miara. Homogenization and shape sensitivity of microstructures for design of piezoelectric bio-materials. *Mechanics of Advanced Materials and Structures*, 13 (6):473–485, 2006.

[41] P. J. Rousseeuw. Silhouettes: a graphical aid to the interpretation and validation of cluster analysis. *Journal of computational and applied mathematics*, 20:53–65, 1987.

[42] Y. Sakamoto, M. Ishiguro, and G. Kitagawa. Akaike information criterion statistics. 1986.

[43] A. Saltelli and P. Annoni. How to avoid a perfunctory sensitivity analysis. *Environmental Modelling & Software*, 25(12):1508–1517, 2010.

[44] A. Saltelli, K. Chan, E. M. Scott, et al. *Sensitivity analysis*, volume 1. Wiley New York, 2000.

[45] A. Saltelli, M. Ratto, T. Andres, F. Campolongo, J. Cariboni, D. Gatelli, M. Saisana, and S. Tarantola. *Global sensitivity analysis: the primer*. John Wiley & Sons, 2008.

[46] F. Schneider, T. Fellner, J. Wilde, and U. Wallrabe. Mechanical properties of silicones for MEMS. *Journal of Micromechanics and Microengineering*, 18(6):065008, 2008.

[47] B. Scholkopf, S. Mika, C. J. C. Burges, P. Knirsch, K.-R. Muller, G. Ratsch, and A. J. Smola. Input space versus feature space in kernel-based methods. *IEEE Transactions on Neural Networks*, 10(5):1000–1017, 1999.

[48] P. Seuntjens, D. Mallants, J. Šimůnek, J. Patyn, and D. Jacques. Sensitivity analysis of physical and chemical properties affecting field-scale cadmium transport in a heterogeneous soil profile. *Journal of Hydrology*, 264(1–4):185 – 200, 2002.

[49] I. M. Sobol. Sensitivity estimates for nonlinear mathematical models. *Mathematical Modelling and Computational Experiments*, 1(4):407–414, 1993.

[50] I. Y. M. Sobol'. On the distribution of points in a cube and the approximate evaluation of integrals. *Zhurnal Vychislitel'noi Matematiki i Matematicheskoi Fiziki*, 7(4):784–802, 1967.

[51] S. H. Song, G. H. Paulino, and W. G. Buttlar. A bilinear cohesive zone model tailored for fracture of asphalt concrete considering viscoelastic bulk material. *Engineering Fracture Mechanics*, 73(18):2829–2848, 2006.

[52] M. L. Stein. *Interpolation of spatial data: some theory for kriging.* Springer Science & Business Media, 2012.

[53] V. Studer, G. Hang, A. Pandolfi, M. Ortiz, W. F. Anderson, and S. R. Quake. Scaling properties of a low-actuation pressure microfluidic valve. *Journal of Applied Physics*, 95 (1):393–398, 2004.

[54] J. A. K. Suykens and J. Vandewalle. Least squares support vector machine classifiers. *Neural Processing Letters*, 9(3):293–300, 1999.

[55] B. C. Taylor, J. L. Stott, M. A. Thurmond, and J. P. Picanso. Alteration in lymphocyte subpopulations in bovine leukosis virus-infected cattle. *Veterinary Immunology and Immunopathology*, 31(1-2):35–47, 1992.

[56] U. Teipel. *Energetic materials: particle processing and characterization.* John Wiley & Sons, 2006.

[57] V. Tvergaard and J. W. Hutchinson. The influence of plasticity on mixed mode interface toughness. *Journal of the Mechanics and Physics of Solids*, 41(6):1119–1135, 1993.

[58] H. Wadell. Volume, shape, and roundness of quartz particles. *The Journal of Geology*, 43 (3):250–280, 1935.

[59] S. M. Walley, J. E. Field, and M. W. Greenaway. Crystal sensitivities of energetic materials. *Materials Science and Technology*, 22(4):402–413, 2006.

[60] D. J. Walters, D. J. Luscher, V. Manner, J. D. Yeager, and B. M. Patterson. Investigating deformation and mesoscale void creation in hmx based composites using tomography based grain scale finite element modeling. *Bulletin of the American Physical Society*, 2017.

[61] D.-X. Wang, S.-S. Chen, Y.-Y. Li, J.-Y. Yang, T.-Y. Wei, and S.-H. Jin. An investigation into the effects of additives on crystal characteristics and impact sensitivity of RDX. *Journal of Energetic Materials*, 32(3):184–198, 2014.

[62] X. Wang, Y. Wu, F. Huang, T. Jiao, and R. J. Clifton. Mesoscale thermal-mechanical analysis of impacted granular and polymer-bonded explosives. *Mechanics of Materials*, 99:68 – 78, 2016.

[63] Y.-Q. Wu and F.-L. Huang. A micromechanical model for predicting combined damage of particles and interface debonding in PBX explosives. *Mechanics of Materials*, 41(1):27 – 47, 2009.

[64] M. Yu, P. Zhu, and Y. Ma. Global sensitivity analysis for the elastic properties of hollow spheres filled syntactic foams using high dimensional model representation method. *Computational Materials Science*, 61:89 – 98, 2012.

[65] Z. Zhou, P. Chen, F. Huang, and S. Liu. Experimental study on the micromechanical behavior of a PBX simulant using SEM and digital image correlation method. *Optics and Lasers in Engineering*, 49(3):366 – 370, 2011.

[66] T. I. Zohdi. Modeling and simulation of laser processing of particulate-functionalized materials. *Archives of Computational Methods in Engineering*, 24(1):89–113, 2017.